# Mechanics of adhesion in MEMS — a review

Y.-P. ZHAO [1,*], L. S. WANG [1,†] and T. X. YU [2]

[1] *State Key Laboratory of Nonlinear Mechanics (LNM), Institute of Mechanics, Chinese Academy of Sciences, Beijing 100080, China*
[2] *Department of Mechanical Engineering, Hong Kong University of Science and Technology, Clear Water Bay, Kowloon, Hong Kong SAR, China*

**Abstract**—A review is presented of the mechanics of microscale adhesion in microelectromechanical systems (MEMS). Some governing dimensionless numbers such as Tabor number, adhesion parameter and peel number for microscale elastic adhesion contact are discussed in detail. The peel number is modified for the elastic contact between a rough surface in contact with a smooth plane. Roughness ratio is introduced to characterize the relative importance of surface roughness for microscale adhesion contact, and three kinds of asperity height distributions are discussed: Gaussian, fractal, and exponential distributions. Both Gaussian and exponential distributions are found to be special cases of fractal distribution. Casimir force induced adhesion in MEMS, and adhesion of carbon nanotubes to a substrate are also discussed. Finally, microscale plastic adhesion contact theory is briefly reviewed, and it is found that the dimensionless number, plasticity index of various forms, can be expressed by the roughness ratio.

*Keywords*: Microscale adhesion contact; Tabor number; adhesion parameter; peel number; surface roughness; fractal distribution; surface energy; surface force.

## 1. INTRODUCTION

Scale effect is one of the fundamental issues in building MEMS [1]. The most challenging issues lie in the fact that the surface-to-volume ratio increases when the MEMS dimensions decrease. The types of forces that influence microscale devices are different from those that influence devices with conventional scale. This is because the size of a physical system bears a significant influence on the

---

*To whom correspondence should be addressed. Phone: 86-10-6265 8008. Fax: 86-10-6256 1284. E-mail: yzhao@lnm.imech.ac.cn

†Currently at Biomedical Engineering Department, University of California, Irvine, CA, USA.
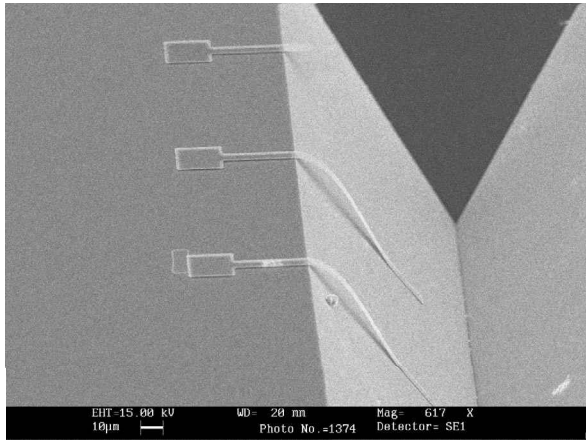
**Figure 1.** Stiction of microcantilevers to substrate.
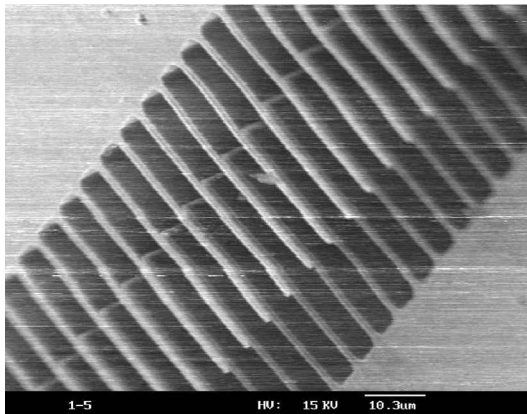


**Figure 2.** Adhesion between fingers of a comb structure in a microaccelerometer.

physical phenomena that dictate the dynamic behavior of that system. For example, larger-scale systems are influenced by inertia effects to a much greater extent than smaller-scale systems, while smaller systems are more influenced by surface effects. Therefore, surface effect induced strong adhesion, friction and wear are major problems limiting both the fabrication yield and operation lifetime of many MEMS devices [2, 3]. Strong adhesion is generally caused by capillary, electrostatic, van der Waals forces, and other kinds of 'chemical' forces [4, 5]. Stiction is a term that has been applied to the unintentional adhesion of compliant microstructure surfaces when restoring forces are unable to overcome interfacial forces. The stiction problem of MEMS can be divided into two categories: release-related stiction and in-use stiction. Release-related stiction occurs during the sacrificial layer removal process in fabrication of microstructures, and such stiction is caused primarily by capillary forces. In-use stiction usually occurs upon exposure of successfully released microstructures to a humid environment. Figure 1 illustrates

(a)                                                            (b)
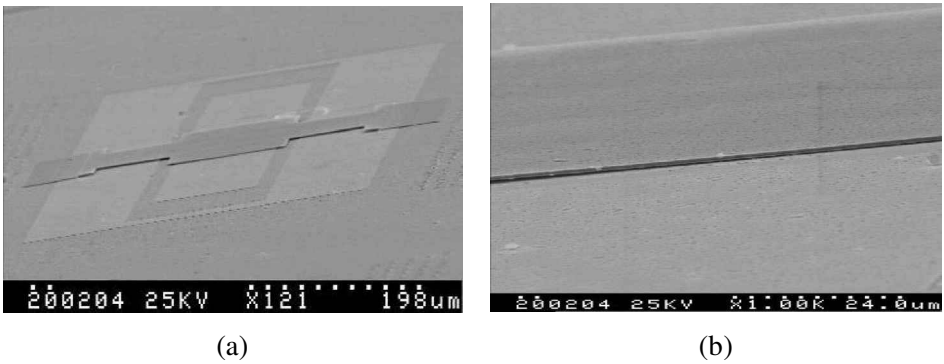
**Figure 3.** SEM of adhered RF-MEMS switch to substrate: (a) low magnification; (b) high magnification.
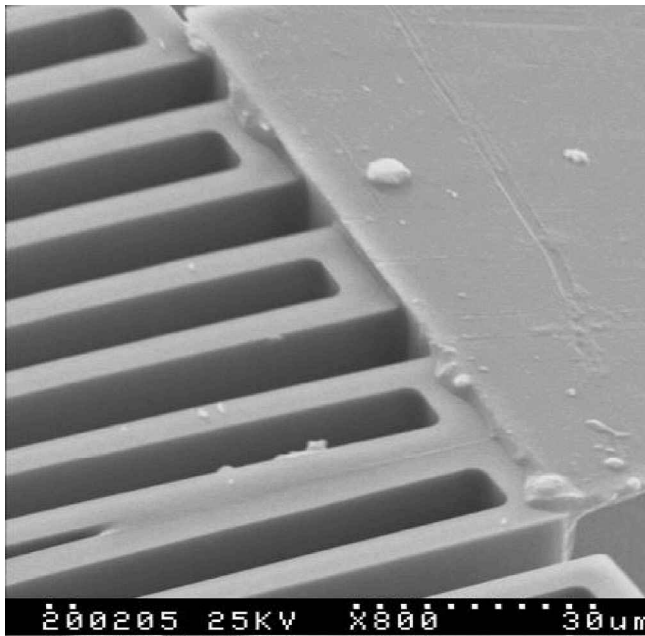


**Figure 4.** Adhesion of microstructural members in an accelerometer after impact loading.

stiction of microcantilevers to the substrate. Figure 2 shows the adhesion between the fingers of a comb structure in a micromachined accelerometer. Figure 3 shows the adhesion (stiction) of an RF-MEMS switch to the substrate [6]. As a result, adhesion (stiction) can be a fundamental catastrophic failure that deserves a great deal of study [7, 8].

Adhesion (stiction) can also be caused by inertia (shock, rapid air flow) forces. Figure 4 shows the adhesion of microstructural members in a micromachined accelerometer after impact loading.

Since adhesion (stiction) failure is one of the most important issues concerning reliability of MEMS, the microscale elastic adhesion contact theory will be reviewed in Section 2. Emphasis will be placed on some governing dimensionless numbers, namely, Tabor number, adhesion parameter and peel number. The effect of surface roughness will also be discussed in detail, and three kinds of roughness distributions will be treated, namely, Gaussian, exponential and fractal distributions. Microscale plastic adhesion contact will be briefly reviewed in Section 3.

## 2. MICROSCALE ELASTIC ADHESION CONTACT THEORIES

Early experiments with a soft rubber sphere in contact with glass revealed the importance of adhesion and led to the development of mechanical theories of adhesion of elastic spherical surfaces [9], which enable Hertzian contact areas to be reliably calculated in the presence of adhesion. The theory shows that the relative magnitude of the adhesion varies inversely with the product of the contact size and the equivalent elastic modulus of the two surfaces. In the experiments with rubber, the contact size is comparatively large (millimeters), but the equivalent elastic modulus is small. In the experiments with nanoprobe instruments, the equivalent elastic modulus is large but the contact size is very small (nanometers). It has been known for a long time that the surface roughness is very important in the magnitude of the force required to separate two materials after they had been brought into contact. Development of sophisticated understanding of adhesion between solid–solid surfaces is important, for example, in microelectronics and MEMS technologies.

All the theories reviewed in this section are continuum elastic theories and hence assume that no plastic deformation occurs.

### 2.1. Tabor number

Bradley in 1932 showed that if two rigid (incompressible) spheres of radii $R_1$ and $R_2$ were placed in contact, they adhered with a force [10]

$$P_c = 2\pi R W_a, \tag{1}$$

where $R = R_1 R_2/(R_1 + R_2)$ is the equivalent radius and $W_a = \gamma_1 + \gamma_2 - \gamma_{12}$ is the Dupré adhesion or work of adhesion, with $\gamma_1$ and $\gamma_2$ being the surface energies of the two spheres and $\gamma_{12}$ being the interface energy. Subsequently by modifying the classic Hertz contact theory which takes into account neither surface forces nor adhesion, Johnson, Kendall and Roberts (JKR) showed that the force required to separate the spheres was [11]

$$P_c = \frac{3}{2}\pi R W_a, \tag{2}$$

which is independent of the elastic modulus and so appears to be universally applicable and therefore to conflict with Bradley's view. According to JKR theory

the elastic modulus, while having an effect on the contact area, has no effect on the adhesion force. The discrepancy between the Bradley and JKR theories was explained by Tabor [12], who identified a governing dimensionless parameter called the Tabor number $(\mu)$

$$\mu = \left( \frac{RW_a^2}{E^{*2}\varepsilon^3} \right)^{1/3}, \tag{3}$$

where $E^*$ is the equivalent Young's modulus given by $1/E^* = (1 - v_1^2)/E_1 + (1 - v_2^2)/E_2$, $\varepsilon$ is the interatomic spacing, $E_{1,2}$ and $v_{1,2}$ are Young's modulus and Poisson's ratio of the two spheres, respectively. Tabor noted the existence of a neck around the contact area in the JKR contact, with a height of the order

$$h^* = \left( \frac{RW_a^2}{E^{*2}} \right)^{1/3}. \tag{4}$$

The Tabor number is thus the ratio of the neck height to the intermolecular spacing $\varepsilon$. This number is also a measure of the magnitude of the elastic deformation, which depends on the range of surface forces [13]; thus, contact bodies with small Tabor number are easier to adhere to each other. Subsequently Muller *et al.* [14] performed a complete numerical solution in terms of surface forces rather than surface energy, and confirmed that the Tabor number $(\mu)$ did indeed govern the transition from Bradley model to JKR model [14].

For small $\mu$ (less than say 0.1) elastic deformation is negligible and the Bradley analysis provides a good approximation; for large $\mu$ (greater than say 5) the JKR theory is applicable [13]. The numerical analysis by Greenwood [15] shows that the load-approach curves become S-shaped for $\mu$ values greater than one, leading to jumps in and out of contact. It is pointed out by Muller *et al.* [14] that the JKR equations describe the behavior well for values of $\mu$ of 3 or more. To the authors' knowledge, there is no general agreement that the JKR theory is valid for $\mu \geqslant 3$ or $\mu > 5$.

A map (as shown in Fig. 5) for the contact of elastic spheres was constructed by Johnson and Greenwood [16]. Such map permits contact model selection based on the material properties [17, 18]. This map is also called 'adhesion map' [17]. It is noted that adhesion between elastic surfaces can be expressed in terms of two dimensionless parameters: Tabor number $\mu$ (or elasticity parameter $\lambda = 1.16\mu$) and $\bar{P}$, which expresses the ratio of the external load to the magnitude of the adhesion force.

There is no agreement on the best form for Tabor number [15], so a conversion factors are given in Table 1. Estimated values of elasticity parameter $(\lambda)$ from a few published experiments are given in Table 2 [17].
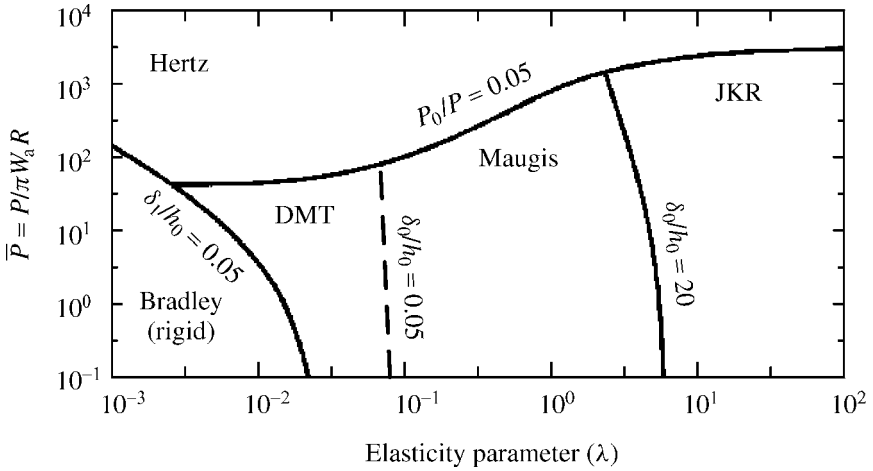
**Figure 5.** Map of the elastic behavior of bodies. $\bar{P}$ is the ratio between the total load and the adhesion part of the load. When adhesion is negligible, the bodies fall in the Hertz limit. $\delta_1$ is the elastic compression, and $h_0$ is the equilibrium distance. When $\delta_1 \ll h_0$, the bodies are rigid and follow Bradley theory. $\delta_0$ is the deformation due to adhesion. When the adhesion is small the behavior of materials is described by the Derjaguin, Muller and Toporov (DMT) theory [19], whilst the JKR theory predicts the behavior of highly adhesive bodies. The Maugis theory [20] (also called Maugis–Dugdale theory) fits the intermediate region, Dugdale potential is used in the Maugis theory to model the separation energy of a single asperity contact [21].

**Table 1.**
Conversion table for Tabor number

| Symbol and equation | Conversion | References |
|---|---|---|
| $\mu = \left( \dfrac{R W_a^2}{E^{*2} \varepsilon^3} \right)^{\frac{1}{3}}$ | | [12, 14] |
| $\mu_T = \left( \dfrac{6\pi^2 R W_a^2}{E^{*2} \varepsilon^3} \right)^{\frac{1}{3}}$ | $\mu_T = 3.898\mu$ | [13] |
| $\mu_D = \dfrac{32}{3\pi} \left( \dfrac{2 R W_a^2}{\pi E^{*2} \varepsilon^3} \right)^{\frac{1}{3}}$ | $\mu_D = 2.921\mu$ | [13] |
| $\lambda = \left( \dfrac{9}{2\pi} \dfrac{R \sigma_0^3}{E^{*2} W_a} \right)^{\frac{1}{3}}, \quad \sigma_0 = \dfrac{16}{9\sqrt{3}} \dfrac{W_a}{\varepsilon}$ | $\lambda = 1.157\mu$ | [18] |
| $\lambda' = \dfrac{W_a}{2E^*} \left( \dfrac{R}{\varepsilon^3} \right)^{\frac{1}{2}}$ | $\lambda' = 0.5\mu^{3/2}$ | [20] |

**Table 2.**
Estimates of elasticity parameter $\lambda$ [17]

| Material system | $\lambda$ |
|---|---|
| Polyurethane sphere with glass substrate [22] | $10^3$ |
| Two mica surfaces in contact using Surface Force Apparatus [23] | 50 |
| 8 $\mu$m diameter pentaerythrite (PET) monofilaments in contact [24] | 12 |
| 1.0 $\mu$m diameter carbon particles in contact | 0.5–1.5 |
| Platinum-coated AFM tip with mica in UHV [25] | 0.8 |
| Si AFM tip with NbSe$_2$ in UHV [26] | 0.2–0.3 |

For adhesion between bodies of the same material, $W_a$, $E^*$ and $\varepsilon$ are fixed, and as a result, Tabor number in equation (3) scales as

$$\mu \sim R^{1/3}. \tag{5}$$

Equation (5) illustrates that the smaller the equivalent sphere radius, the easier the two bodies will adhere to each other. For the same equivalent radius $R$, $\mu$ (or $\lambda$) is small for hard materials and large for soft materials.

## 2.2. Surface roughness and adhesion parameter

At microscale, no surface used in MEMS structures can be regarded as being smooth. The resistance to motion offered by rough surfaces is larger than that given by the equations for a smooth surface. On the other hand, the roughness plays a major role in preventing adhesion or stiction [27].

To study the relative importance of surface roughness, a dimensionless number, termed roughness ratio, is introduced as follows

$$\Xi = \frac{\sigma}{L}, \tag{6}$$

where $\sigma$ is the characteristic dimension of the asperities on the rough surface (e.g. the standard deviation of the distribution of asperity heights), $L$ is the characteristic dimension of a microstructure contacting the asperities. In the study of nano/micro-tribology, $L$ can be considered the radius of curvature of the asperity $R$, or, alternatively, as the correlation distance between asperities. It should be pointed out that roughness ratio has been widely used in fluid dynamics to determine the influence of wall roughness on turbulence [28].

Another governing dimensionless number, called adhesion parameter $\theta$, was introduced by Fuller and Tabor [29] governing the adhesion between a rough and a smooth surface

$$\theta = \frac{E^*}{W_a} \sqrt{\frac{\sigma^3}{R}}, \tag{7}$$

where $\sigma$ is the standard deviation of the distribution of asperity heights, and $R$ is the radius of curvature of the asperity tips. The adhesion parameter represents the

statistical average of the competition between the compressive forces exerted by the higher asperities, which tend to separate the surfaces and the adhesion between the lower asperities, which hold the surfaces together. When the adhesion parameter is small the adhesion dominates and the adhesion is high; as the surface roughness, and hence the adhesion parameter, increases the high asperities push the surfaces apart and the adhesion is reduced. Using the roughness ratio in equation (6), the adhesion parameter in equation (7) can be recast as (remembering that $L$ can be considered as $R$)

$$\theta = \frac{E^*\sigma}{W_a}\Xi^{1/2}. \tag{8}$$

Using the adhesion parameter $\theta$ as a measure, three kinds of wafer contacts can be identified in direct wafer bonding with respect to their bondability [30], viz., the nonbonding regime ($\theta \geqslant 12$), the bonding regime ($\theta \leqslant 1$), and the transition regime ($1 < \theta < 12$).

## 2.3. Adhesion of microstructures to the substrate

*2.3.1. Peel number.*    To study the adhesion of movable MEMS microstructures to the substrate, a dimensionless number, termed peel number, was proposed by Mastrangelo and Hsu in [31]. The peel number, $N_P$, is the ratio of elastic strain energy stored in the deformed microstructure to the work of adhesion between the microstructure and the substrate. If $N_P > 1$, the restored elastic strain energy is greater than the work of adhesion, and the microstructure will not adhere to the substrate. If, on the other hand, $N_P \leqslant 1$, the deformed microstructure does not have enough energy to overcome the adhesion between the beam and the substrate.

For a long slender cantilever of thickness $t$ and elastic modulus $E$ suspended at a distance $h$ from the substrate, illustrated in Fig. 6a, the peel number is [31]

$$N_P = \frac{3Et^3h^2}{2s^4W_a}, \tag{9}$$

where $s$ is the crack length, and again $W_a$ is the work of adhesion between the cantilever and the substrate. For a short cantilever beam with just its tip adhered to the substrate, shown in Fig. 6b, the corresponding peel number is [31]

$$N_P = \frac{3Et^3h^2}{8L^4W_a}. \tag{10}$$

For a doubly clamped beam, and suspended square and circular plates, the residual stress, $\sigma_R$, must be considered, and their peel numbers are [31]

$$N_P = \frac{128Et^3h^2}{5L^4W_a}\left[1 + \frac{4\sigma_R L^2}{21Et^2} + \frac{256}{2205}\left(\frac{h}{t}\right)^2\right]$$

(doubly clamped beam), $\tag{11}$
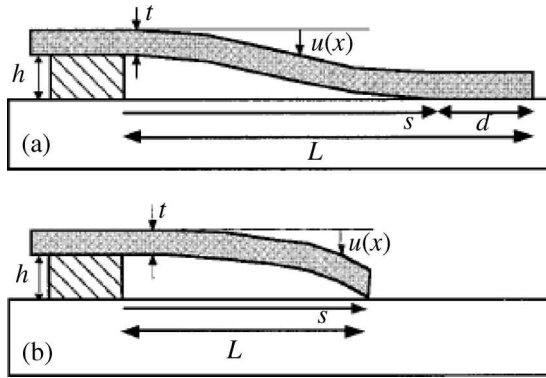
**Figure 6.** (a) S-shaped cantilever adhered to the substrate over a distance $d$; (b) arc-shaped cantilever adhered to the substrate only very near its tip [8].

$$N_P = \frac{186Et^3h^2}{(1-v^2)w^4W_a}\left[1 + \frac{27(1-v^2)\sigma_R w^2}{310Et^2} + \frac{12}{31}\left(\frac{h}{t}\right)^2\right]$$

(suspended square plate), \hfill (12)

$$N_P = \frac{40Et^3h^2}{3(1-v^2)R_P^4 W_a}\left[1 + \frac{51(1-v^2)\sigma_R R_P^2}{160Et^2}\right]$$

(suspended circular plate), \hfill (13)

where $v$ is Poisson's ratio, $L$, $w$ and $R_P$ are the length of the doubly clamped beam, width of the square plate and radius of the circular plate, respectively.

The maximum dimensions of the microstructures (length of cantilever or doubly clamped beam, width of square plate, and radius of circular plate) that will not stick to the substrate can be obtained from equations (10)–(13) using the threshold condition $N_P = 1$, i.e. the stored elastic strain energy is equal to the adhesion. From equation (10), the maximum cantilever length that will not adhere to the substrate can be determined as

$$L_{max} = \left(\frac{3Et^3h^2}{8W_a}\right)^{1/4}.$$ \hfill (14)

From equations (11)–(13), the maximum length, width and radius of the fixed-fixed beam, square plate and circular plate are expressed in the same form as follows

$$L_{max}, w_{max}, (R_P)_{max} = \left(\frac{b + \sqrt{b^2 + 4c}}{2}\right)^{1/2}.$$ \hfill (15)

The corresponding values of $b$ and $c$ in equation (15) for different microstructures are presented in Table 3.

**Table 3.**
Coefficients in equation (15) for different microstructures

| Microstructure | $b$ | $c$ |
|---|---|---|
| Doubly clamped beam | $\dfrac{512}{105}\dfrac{\sigma_R h^2 t}{W_a}$ | $\dfrac{128}{5}\left[1+\dfrac{256}{2205}\left(\dfrac{h}{t}\right)^2\right]\dfrac{Et^3 h^2}{W_a}$ |
| Square plate | $\dfrac{5022}{301}\dfrac{\sigma_R h^2 t}{W_a}$ | $\left[1+\dfrac{12}{31}\left(\dfrac{h}{t}\right)^2\right]\dfrac{186Et^3 h^2}{(1-v^2)W_a}$ |
| Circular plate | $\dfrac{17}{4}\dfrac{\sigma_R h^2 t}{W_a}$ | $\dfrac{40Et^3 h^2}{3(1-v^2)W_a}$ |

*2.3.2. Influence of surface roughness on adhesion of microstructures.* For simplicity and without loss of generality, we consider the elastic contact of a smooth surface and a rough surface (illustrated in Fig. 7). The surface roughness is represented by asperities, which are modeled as spherical caps with the same radius of curvature $R$, and the heights of these asperities obey the Gaussian distribution.

Suppose the asperity density, defined as the number of asperities per unit area, is $N$, then the number of asperities per unit area in contact with the smooth surface is

$$n = N \int_d^\infty \varphi(z)\,\mathrm{d}z, \tag{16}$$

where $d$ is the separation of the smooth plane with respect to the reference plane of mean asperity height. If the peak height $z$ of asperities above the mean line has a Gaussian distribution $\varphi(z)$, one has

$$\varphi(z) = \frac{1}{\sqrt{2\pi}\sigma}\exp\left(-\frac{z^2}{2\sigma^2}\right). \tag{17}$$

The probability that an asperity has a height between $z$ and $z + \mathrm{d}z$ above the plane defined by the mean asperity height is $\varphi(z)\,\mathrm{d}z$.

Since silicon has a high elastic modulus, the DMT model [19] is adopted here. The total compressive load per unit area is given by

$$P = \frac{ENR^{1/2}}{\sqrt{2\pi}\sigma}\int_d^\infty (z-d)^{3/2}\exp\left(-\frac{z^2}{2\sigma^2}\right)\mathrm{d}z - \frac{2\pi W_a NR}{\sqrt{2\pi}\sigma}\int_d^\infty \exp\left(-\frac{z^2}{2\sigma^2}\right)\mathrm{d}z. \tag{18}$$

The maximum extension of a single asperity when peeling takes place is

$$\delta_C = \frac{1}{3R}\left(\frac{3RP_C}{E}\right)^{2/3}, \tag{19}$$
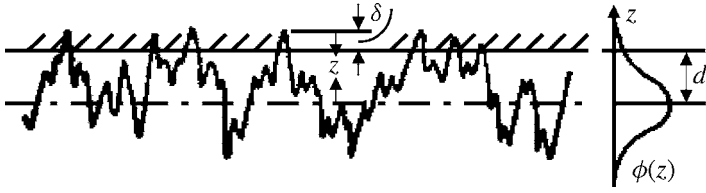
**Figure 7.** Microscale representation of elastic contact between smooth and randomly rough surfaces.

and the adhesion parameter is given by $\theta = E\sigma^{3/2}/(R^{1/2}W_a) = (\sigma/\delta_C)^{3/2}$. Introducing dimensionless variables $s = d/\sigma$ and $x = z/\sigma$, equation (18) is then transformed to a dimensionless form as follows [30]

$$P^* = \frac{P}{W_a/\sigma}$$

$$= RN\sigma \left[ \frac{4\theta}{3\sqrt{2\pi}} \int_s^\infty (z-s)^{3/2} \exp\left(-\frac{x^2}{2}\right) dx - \sqrt{2\pi} \int_s^\infty \exp\left(-\frac{x^2}{2}\right) dx \right]. \tag{20}$$

The equilibrium separation $s_e$ can be determined by setting $P^* = 0$. The equilibrium separation is the distance where the stored strain energy in the MEMS structure and the adhesion energy are balanced.

The mechanical work needed for separating two bonded surfaces from equilibrium separation to infinity is

$$U'_{Sp} = \int_{s_e}^\infty P\, ds. \tag{21}$$

The dimensionless separation work is then recast into the form

$$U^* = \frac{U'_{Sp}}{W_a} = RN\sigma \int_{s_e}^\infty \left[ \frac{4\theta}{3\sqrt{2\pi}} \int_s^\infty (x-s)^{3/2} \exp\left(-\frac{x^2}{2}\right) dx \right.$$

$$\left. - \sqrt{2\pi} \int_s^\infty \exp\left(-\frac{x^2}{2}\right) dx \right] ds. \tag{22}$$

It is noted that for an actual surface the following relation exists

$$\sigma RN \cong C, \tag{23}$$

where the value of constant $C$ is between 0.05 and 0.1 [27, 30].

It is seen from equations (20) and (23) that the effective adhesion, $W'_C$, considering the surface roughness is given by

$$W'_C = f(\theta)W_a, \tag{24}$$

where

$$f(\theta) = C \int_{s_e}^{\infty} \left[ \frac{4\theta}{3\sqrt{2\pi}} \int_{s}^{\infty} (x-s)^{3/2} \exp\left(-\frac{x^2}{2}\right) dx - \sqrt{2\pi} \int_{s}^{\infty} \exp\left(-\frac{x^2}{2}\right) dx \right] ds, \tag{25}$$

is a dimensionless roughness function reflecting the influence of surface roughness on adhesion (Fig. 8).

Consider the adhesion of an S-shaped cantilever beam (illustrated in Fig. 6a) with a rough substrate. The detachment energy of the cantilever from the substrate is

$$U_S = w(L-s)W'_C = w(L-s)f(\theta)W_a,$$

and the elastic strain energy is

$$U_E = \frac{EI}{2} \int_0^s \left(\frac{d^2u}{dx^2}\right)^2 dx = \frac{6EIh^2}{s^3}.$$

The corresponding peel number for cantilever beam adhesion to a rough surface is determined by the equilibrium condition

$$\frac{d(U_S + U_E)}{ds} = 0$$

as

$$\bar{N}_P = \frac{N_P}{f(\theta)}, \tag{26}$$

where $N_P$ is the peel number for smooth contact (equation (9) or equation (10)), $\bar{N}_P$ is the peel number considering the rough contact, and $f(\theta)$ is the dimensionless roughness function defined in equation (25). Equation (26) indicates [32] that the adhesion of a cantilever beam with a rough substrate is reduced with increasing adhesion parameter, $\theta$. The modification of peel number for doubly clamped beam, and suspended square and circular plates with surface roughness can be done in the same manner. The design parameters in equations (14) and (15) should be modified accordingly, for example, the maximum cantilever beam length that will not adhere to the substrate can be modified to

$$L'_{max} = \left( \frac{3Et^3h^2}{8W_a f(\theta)} \right)^{1/4}.$$

The difference between $L'_{max}$ and $L_{max}$ in equation (14) is $f(\theta)$. Noticing the fact that the dimensionless roughness function is less than 1 by referring to Fig. 8, then $L'_{max}$ is always larger than $L_{max}$.
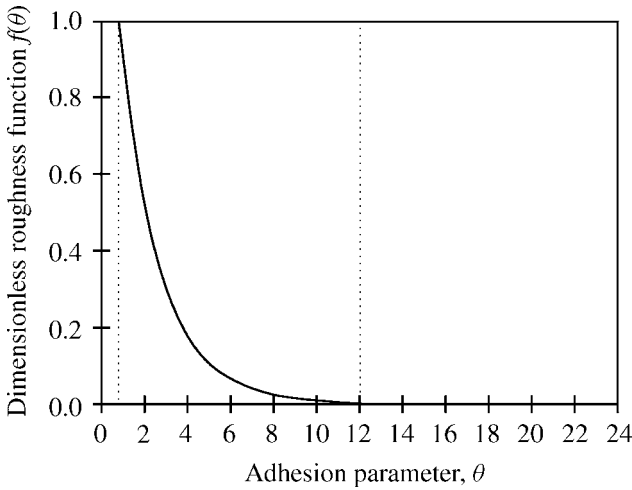
**Figure 8.** Influence of adhesion parameter on the dimensionless roughness function $f(\theta)$, which decreases monotonically with the adhesion parameter $\theta$ [30].

### 2.4. Adhesion of rough surfaces with fractal geometry

Most of the literature on rough surfaces assumes that the height distributions are Gaussian, which is too restrictive for many important applications of MEMS. As an illustration, Fig. 9a shows the Atomic Force Microscope (AFM) profile of the rough surface of Single Crystal Silicon (SCS) etched by KOH solution. The height of the surface asperities (shown in Fig. 9b) does not obey Gaussian distribution.

A model developed by Chow [33] describes the adhesion between deformable fractal surfaces with distribution of asperity heights as

$$\psi(z) = \psi_0 \exp\left[-\alpha\left(\frac{z}{\sigma}\right)^{1/\alpha}\right], \quad 0 < \alpha \leqslant 1, \tag{27}$$

where $\alpha$ is the roughness exponent, $\sigma$ is the standard deviation of the asperity heights, and

$$\psi_0 = \left[\sigma \int_0^\infty \exp\left(-\alpha u^{1/\alpha}\right) du\right]^{-1} = \frac{1}{\sigma\alpha^{1-\alpha}\Gamma(\alpha)}, \tag{28}$$

where $\Gamma$ is the gamma function. When $\alpha = 1/2$, one obtains the Gaussian distribution function from the above two equations, and the exponential distribution is obtained when $\alpha = 1$. The radius of curvature of asperities $R$ is given as

$$\frac{1}{R} = \frac{2\sigma}{\xi^2}, \tag{29}$$

where $\xi$ is the correlation length of the self-affine fractal surface parallel to the surface. The relative adhesion (or pull-off force) for rough surfaces in contact can

(a)



(b)
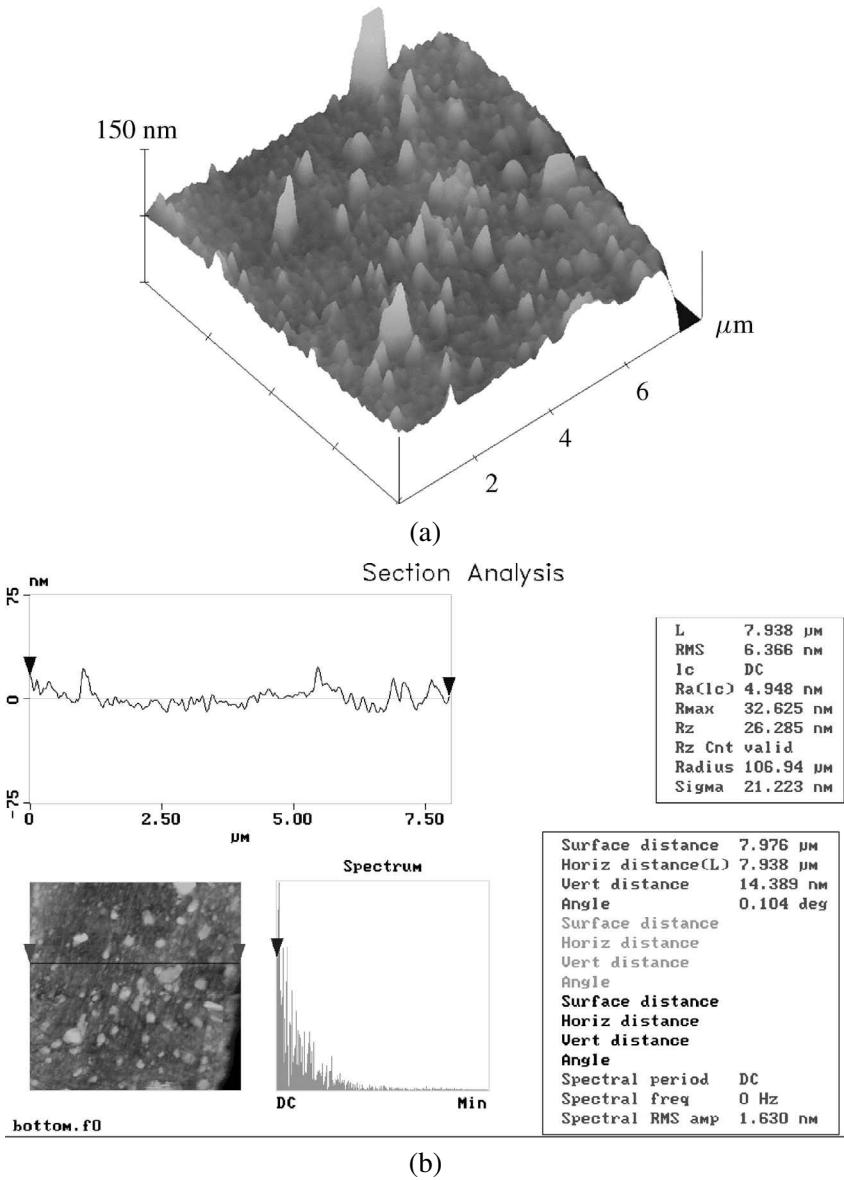
**Figure 9.** (a) Surface roughness profile of single crystal silicon (8 $\mu$m $\times$ 8 $\mu$m) obtained by atomic force microscope (AFM); (b) a cross-sectional analysis of part of the region of surface shown in (a), showing roughness distribution determined by AFM.

be written as

$$\frac{P}{P_c} = -\frac{1}{\alpha^{1-\alpha}\Gamma(\alpha)} \int_0^\infty f\left(|\beta s - 1|\right) \exp\left(-\alpha s^{1/\alpha}\right) ds, \tag{30}$$
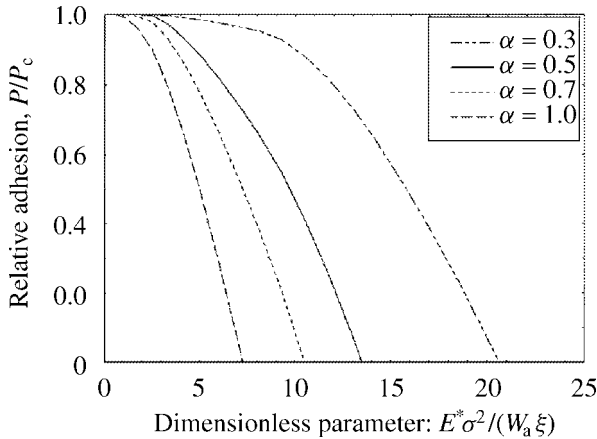
**Figure 10.** Influence of dimensionless parameter $E^*\sigma^2/(W_a\xi)$ on relative adhesion in equation (30) [33].

where $P_c = (3/2)\pi W_a R$, which is the same as that in equation (2). A dimensionless parameter, $\beta$, is introduced

$$\beta = 2\left(\frac{4}{3\pi}\frac{E^*\sigma^2}{W_a\xi}\right)^{2/3}, \tag{31}$$

and defined as the ratio between the standard deviation of the asperity heights and the maximum extension of an asperity tip above its undeformed height before separation occurs. The normalized force–displacement relationship is then

$$f(|\beta s - 1|) = \begin{cases} -1, & \text{for } 0 \leqslant |\beta s - 1| < 1, \\ |\beta s - 1|^{3/2} - 2|\beta s - 1|^{3/4}, & \text{for } |\beta s - 1| \geqslant 1. \end{cases} \tag{32}$$

Equations (30)–(32) give quantitative predictions of the adhesion between deformable fractal surfaces (fractal dimension can be calculated using digital data obtained from AFM [34]). Figure 10 shows the effect of roughness exponent $\alpha$ and the dimensionless number $E^*\sigma^2/(W_a\xi)$ on the relative adhesion (equation (30)).

## 2.5. Adhesion by Casimir force

An important feature of the Casimir effect is that even though it is quantum in nature, it predicts a force between macroscopic bodies [35]. This makes the Casimir force relevant in MEMS and Nanoelectromechanical Systems (NEMS); the Casimir force fundamentally influences the performance and yield of NEMS devices [35]. Casimir force actuation for MEMS has been claimed recently by some researchers [36].

The Casimir force has been associated with van der Waals forces. The following comparison between the Casimir and van der Waals forces has been made by Lifshitz [37]:
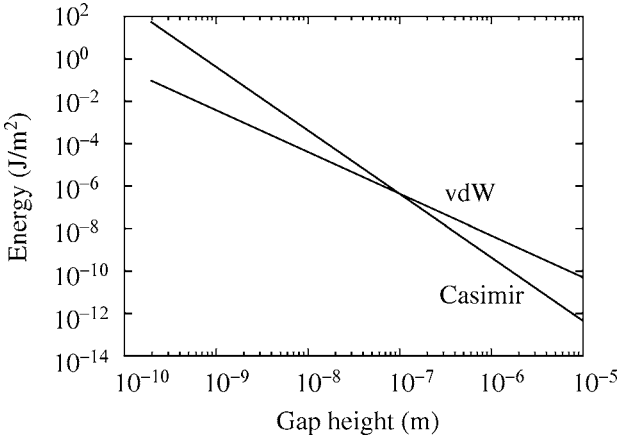
**Figure 11.** Comparison of van der Waals and Casimir forces for thick gold films [38].

(1) van der Waals force: Approximation of perturbation theory applied to electrostatic interaction of two dipoles. This is valid only when separation $a < \lambda$, with $\lambda$ being the retardation length, and corresponds to the transition between the ground and the excited states of the atom. The attraction is proportional to $1/a^3$ and is affected by material properties.

(2) Casimir force: When the separation $a \sim \lambda$ or $a > \lambda$, retardation effects become operative. The attraction is proportional to $1/a^4$ and it is not affected by material properties.

Thus the Casimir forces are in effect at longer distances than the van der Waals forces. Figure 11 shows calculated results of Casimir and van der Waals energies for two thick films [38]:

$$E_{\text{vdW}}(a) = 0.28\frac{\hbar\omega_{\text{p}}}{16\pi\sqrt{2}a^2}, \quad E_{\text{Casimir}}(a) = \frac{\pi^2\hbar c}{720a^3}, \tag{33}$$

where $\hbar$ is the Planck's constant divided by $2\pi$, $\omega_{\text{p}}$ is the plasma frequency, $a$ is the gap height, and $c$ is the speed of light. The crossing point in Fig. 11 is at $\sim$100 nm gap height for $\omega_{\text{p}} = 10^{16}$ Hz. As the surfaces get closer together, van der Waals forces and electron exchange interactions dominate.

The Casimir force acting on two parallel uncharged plates in vacuum is given by [38, 39]

$$F(a) = -\frac{\pi^2}{240}\frac{\hbar c}{a^4}S, \tag{34}$$

where $S \gg a^2$ is the area of plates. Thus movable components in NEMS devices fabricated at distances less than 100 nm between each other often stick together due to strong Casimir force.

Buks and Roukes [40] measured the adhesion between gold surfaces using a micromachined cantilever beam. The adhesion is caused by the Casimir force with

rectangular membrane strip
(thickness $h$)

surface $S$

$x$ $q(x)$

$w(x)$

$w_0$

$L$

edge support     rigid, flat plate
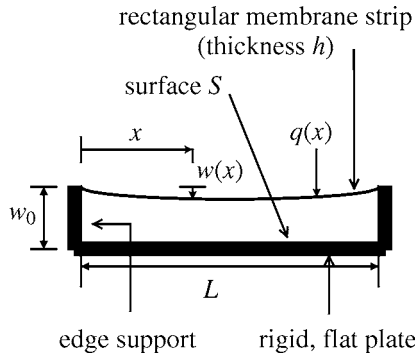
**Figure 12.** Illustration of the Casimir effect between a rectangular membrane strip and the substrate. $w(x)$ is the deflection of the strip, $q(x)$ is the load, and $w_0$ is the initial separation between the strip and the substrate.

a gap of a few micrometers between the cantilever and the substrate. The Casimir force for a small separation is reduced to the nonretarded van der Waals forces [41] with interaction energy per unit area

$$U = -\frac{A}{12\pi a^2},\qquad(35)$$

where $A$ is the Hamaker constant. For the case of Au, it was found [40] that equation (35) was a good approximation for the gap $a < 2$ nm and the Hamaker constant was measured to be $A = 4.4 \times 10^{-19}$ J.

Serry *et al.* [42] studied the criterion for adhesion of a 2 $\mu$m thick highly doped single crystal Si microfabricated rectangular membrane strip with a parallel fixed surface in terms of Casimir force as shown in Fig. 12. Due to proximity to the rigid flat surface $S$ of the bottom plate, the strip is subject to the attractive Casimir force, and deflects into a curved shape. Numerical simulation in [42] showed that for those systems which exhibited adhesion-free stable equilibrium state, the deflection at middle of the strip was always less than $0.48w_0$, with $w_0$ being the initial gap between the rectangular strip and the parallel surface. However, Serry *et al.* [42] do not discuss the building of the structure studied or how the deflection of the strip was measured.

## 2.6. Adhesion of carbon nanotubes to a substrate

Carbon nanotubes not only have remarkable electronic properties but also astonishing mechanical properties. Thus carbon nanotubes are promising materials for application in NEMS.

Because the characteristic dimension of carbon nanotubes is down to nanometers, there is a strong adhesion between carbon nanotubes and substrates due to van der Waals forces. The work of adhesion between a multi-walled carbon nanotube (MWCNT) and $SiO_2$ substrate, $W_{sn} = 2\sqrt{\gamma_{SiO_2}\gamma_g}$, is measured to be approximately
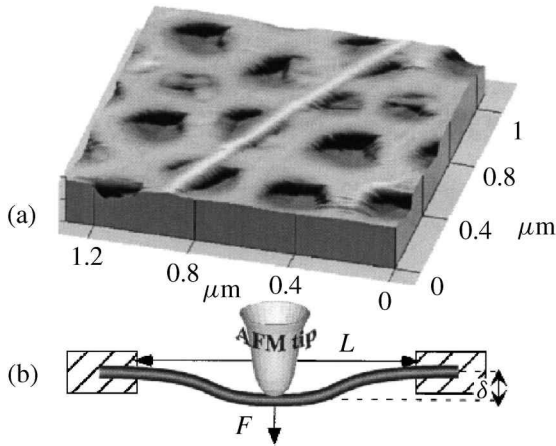
**Figure 13.** (a) 3D AFM image showing adhesion of a carbon nanotube rope of 20 nm diameter to the substrate; (b) measurement of the mechanical behavior of the rope loaded by AFM tip [44].

330 mJ/m$^2$ [43], where $\gamma_g$ is the surface energy of graphite and $\gamma_{SiO_2}$ is the surface energy of SiO$_2$ substrate.

The elastic modulus of a carbon nanotube rope adhered to the polished alumina ultrafiltation membrane (shown in Fig. 13a) has been measured [44] by AFM tip loading (shown in Fig. 13b). Nanotubes occasionally lie over pores with most of the tube in contact with the membrane surface, producing a suspended beam configuration at the nanoscale. The SWNT rope of 20 nm diameter suspends over a 200 nm pore. The AFM tip pushes the rope down towards the pore. It is noted that the adhesion between the carbon nanotube rope and the substrate is strong enough to endure the large deformation of the rope.

## 3. MICROSCALE PLASTIC ADHESION CONTACT THEORIES

### 3.1. Criterion for plastic deformation of microscale contact

Greenwood and Williamson proposed asperity contacts at plastic flow in terms of plasticity index [45], i.e.

$$\psi = \frac{E^*}{H}\sqrt{\frac{\sigma}{R}}, \tag{36}$$

where $E^*$ is the equivalent Young's modulus, $1/E^* = (1 - v_1^2)/E_1 + ((1 - v_2^2)/E_2)$, $H$ is the indentation hardness of the material, $\sigma$ is the standard deviation of the distribution of asperity heights, and $R$ is the radius of curvature of the asperity tips, which are assumed to be spherical. The asperity will behave elastically when $\psi < 0.6$, and plastic flow will occur at the asperity when $\psi > 1$. For $0.6 < \psi < 1$, the contact will be elastoplastic. Hutchins [46] found that for metal surfaces, $\psi$ was in the range $0.1 - 100$ [47]. Using the roughness ratio in equation (6), equation (36)

can be rewritten as

$$\psi = \frac{E^*}{H}\sqrt{\Xi}. \tag{37}$$

It should be noted that equations (36) and (37) are valid for isotropic microcontacts (i.e. the contact area being circle); for an elliptical contact, the plasticity index was modified as follows [48]

$$\Psi = \frac{\pi/2}{\sqrt{E(e)K(e)}}\frac{E^*}{H}\sqrt{\frac{\sigma}{R_m}}, \tag{38}$$

where $e = \sqrt{1 - (a/b)^2}$ is the eccentricity of the ellipse, $a$ and $b$ ($a < b$) are the semi-minor and semi-major radii of contact asperity, respectively, $K(e)$ and $E(e)$ are complete elliptical integrals of the first and second kinds, respectively, $R_m = 2(1/R_x + 1/R_y)^{-1}$ is the mean effective radius of curvature of asperities, $R_x$ and $R_y$ are the effective radii of curvature in the principal $x$ and $y$ planes, respectively. When $a = b$, $E(0) = K(0) = \pi/2$ and $R_m = R$, then equation (38) can be reduced to equation (37). It should be noted that equation (38) can be rewritten as

$$\Psi = \frac{\pi/2}{\sqrt{E(e)K(e)}}\frac{E^*}{H}\sqrt{\Xi_m}, \tag{39}$$

where $\Xi_m$ is the average roughness ratio.

A similar formula [49] for plasticity index was suggested by Onions and Archard [50] as

$$\Psi^* = \frac{E^*}{H}\frac{\sigma}{\beta^*}, \tag{40}$$

where $\beta^*$ denotes the correlation distance between the asperities. One advantage of equation (40) over equation (36) is that $\beta^*$ is easier to measure [51] than $R$. Setting $R = 2\sqrt{\pi}(2.3\beta^*)^2/(9\sigma)$ [52] we find using equation (36) that

$$\Psi = 0.69\Psi^*. \tag{41}$$

It should be noted that equations (36) and (41) are valid for 'sphere-on-plane' contact. The plasticity index for 'cylinder-on-plane' contact, $\Psi_c$, has been suggested recently by Zhao and Talke [53] as follows

$$\Psi_c = \Psi s, \tag{42}$$

where

$$s = \left[\frac{2\sqrt{2}}{\pi}\sqrt{\ln\left(\frac{\pi}{\sqrt{e}}\frac{E^*}{H}\right)}\right]^{-1} \tag{43}$$

is a shape coefficient which is less than unity. The 'cylinder-on-plane' contact can be classified as: (1) largely elastic when $\Psi_c < 0.6$; and (2) largely plastic when $\Psi_c > 1.0$.

To study the steady sliding wear behavior of asperities, a so-called 'repeated sliding plasticity index' was defined by Kapoor *et al.* [54] as

$$\Psi_s = \frac{E^*}{p_s}\sqrt{\frac{\sigma}{R}}, \tag{44}$$

where $p_s$ is the shakedown limit load [54, 55]. Equation (44) can be written as

$$\Psi_s = \frac{E^*}{p_s}\sqrt{\Xi}, \tag{45}$$

where $\Xi = \sigma/R$ is the roughness ratio (equation (6)).

Experimental verification of the Greenwood–Williamson model [45] was carried out by Handzel–Powierza *et al.* [56]. Good agreement was found between the experimental and theoretical results within the range of elastic deformation of the surface roughness and for quasi-isotropic surfaces. The Greenwood–Williamson model does not show agreement with experimental results for loads exceeding approximately half of the yield-point load.

### 3.2. Microscale plastic adhesion contact theory

By using the von Mises yield criterion, Maugis and Pollock [57] derived the approximate plastic initiation condition at the central point of the contact area between a semi-sphere and a semi-infinite plane (shown in Fig. 14) as

$$P + 1.5S_f = 1.1\pi a^2 \sigma_Y, \tag{46}$$

where $P$ is the applied load, $\sigma_Y$ is the yield stress, $a$ is the contact radius, and the surface force $S_f$ is

$$S_f = \sqrt{\frac{3}{2}\pi W_a E^* a^3}. \tag{47}$$

The expression for fully plastic contact given by Chowdhury and Pollock [58] is

$$P + 2\pi W_a R = \pi a^2 H, \tag{48}$$

where $H$ is the hardness of the softer material, $R$ is the radius of curvature of the asperities, and $a$ is the radius of contact area.

Consider the contact between a rough deformable surface and a rigid smooth surface. If the asperity peak height $z$ above the mean line has an exponential distribution $\phi(z)$, we have [58]

$$\phi(z) = \frac{N}{\sigma}\exp\left(-\frac{z}{\sigma}\right), \tag{49}$$

where $N$ is the number of asperities per unit area, and $\sigma$ is the standard deviation of the asperity heights. The condition for fully plastic deformation of an asperity is

$$\frac{P}{A_r} + \frac{W_a}{\sigma} = H, \tag{50}$$
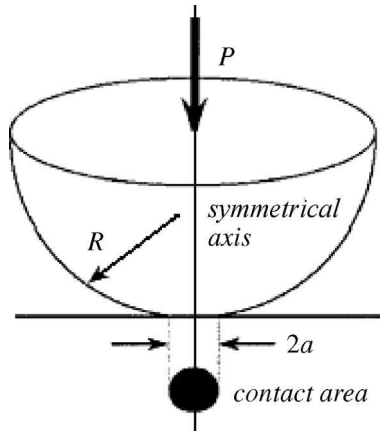
**Figure 14.** Contact between a semi-sphere and a semi-infinite plane. Contact circle with radius $a$ is achieved under the applied force $P$ and surface force $S_f$.

where $A_r = 2\pi n R \sigma$ is the real contact area, $R$ is the radius of curvature of asperities, and $n$ is the number of asperities actually making contact per unit area [58]. It is interesting to note that fully plastic deformation of the asperity occurs in the absence of external applied load provided that

$$\sigma = \frac{W_a}{H}. \tag{51}$$

## 4. DISCUSSION

Because a large surface-to-volume ratio is a distinctive attribute of a micromechanical structure, adhesion (stiction) in both MEMS and NEMS has caused great concerns in both scientific and industrial communities [59, 60]. Therefore, a new field of mechanics, which can be called micro/nano mechanics, has been introduced [61]. *Micro/nano contact mechanics* is one of the main components of this new field. Though continuum adhesion contact mechanics is comparatively well understood, a systematic framework for micro/nano contact mechanics is still lacking.

Plasticity index ($\Psi$) can be used as a criterion for plastic yielding of a single asperity. However, surface energy is not considered for single asperity contact, and it should be noted that surface effect is very important at micro/nano scales because of large surface-to-volume ratio. As a result, equations (36)–(45) should be modified. For an illustration of the importance of adhesion, we consider the indentation of a thin film with a rigid sphere as illustrated in Fig. 14. The classical Hertz theory predicts the contact radius to be

$$a^3 = \frac{3PR(1 - \nu^2)}{4E}, \tag{52}$$
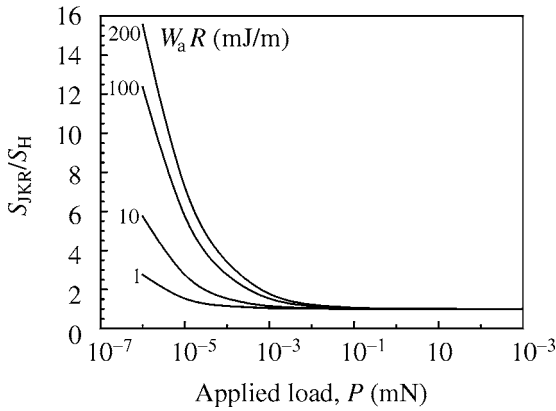
**Figure 15.** Influence of adhesion $W_a$, and applied load on nanoindentation stiffness ratio [62]. The tip radius is $R = 1 \ \mu$m.

where $P$ is the applied load, $R$ is the asperity radius of curvature, $E$ and $\nu$ are the elastic modulus and Poisson's ratio of the film, respectively. The contact stiffness $S_H$ using Hertz contact theory is

$$S_H = 2\frac{E}{1-\nu^2}\left(\frac{3PR(1-\nu^2)}{4E}\right)^{1/3}. \tag{53}$$

If, on the other hand, the JKR model is used, the contact radius produced by both pressure and adhesion is

$$a^3 = \frac{3PR(1-\nu^2)}{4E}\left[P + 3\pi W_a R + \sqrt{6\pi W_a RP + (3\pi W_a R)^2}\right], \tag{54}$$

which leads to the contact stiffness $S_{JKR}$

$$S_{JKR} = 2\frac{E}{1-\nu^2}\left\{\frac{3PR(1-\nu^2)}{4E}\left[P + 3\pi W_a R + \sqrt{6\pi W_a RP + (3\pi W_a R)^2}\right]\right\}^{1/3}. \tag{55}$$

The ratio of equations (55) and (53) is

$$\frac{S_{JKR}}{S_H} = \left\{1 + \frac{3\pi W_a R}{P} + \sqrt{\frac{6\pi W_a R}{P} + \left(\frac{3\pi W_a R}{P}\right)^2}\right\}^{1/3}. \tag{56}$$

Equation (56) shows that the stiffness ratio $S_{JKR}/S_H$ increases with $W_a$ and with decreasing applied load (shown in Fig. 15). In Fig. 15, the nanoindentation tip radius is 1 $\mu$m, and the adhesion between the tip and film is 100 mJ/m$^2$. It is seen from Fig. 15 that the indentation is controlled by the adhesion energy when the load is less than $10^{-3}$ mN [62]. It should be noted that a systematic study is still lacking on the effect of adhesion on nanoindentation test results with other kinds of tip shapes (such as Berkovich, cube corner, etc.), and on plastic flow of asperities.

The size effect is another important issue at micro/nano scale. The size effect of the elastic adhesion contact is reflected by the Tabor number (shown in equation (5)); therefore, for a given material, the horizontal coordinate in Fig. 5 is equivalent to length scale. Adhesion effect will be important for smaller bodies and lighter external loads. For microscale plastic contact, it is interesting that the measured hardness of crystals often exhibits indentation depth effect (or plastic strain gradient effect) when the indentation depth is on the order of micrometer or less [63]. Equation (50) is now modified to [64]

$$\frac{P}{A_r} + \frac{W_a}{\sigma} = H\sqrt{1 + \frac{h_0}{h}},\tag{57}$$

where $h_0$ is the reference indentation depth [63] and $h$ is the actual indentation depth. Indentation depth (or plastic strain gradient) effect is demonstrated by equation (57): the right-hand side value in equation (57) will increase with the decrease of the indentation depth.

The plastic index, $\Psi$, which defines the extent of plastic deformation in elastic–plastic asperity contacts, appears to increase without limit as the sampling length is reduced, showing that the smaller scale asperities will always deform plastically [65]. This scale effect and the experimental results strongly indicate that fractal description of the rough surface and elastic–plastic deformation of asperities would be more appropriate [65]. A fractal model of elastic–plastic contacts between rough surfaces has been developed [66].

The elastic contact of rough surfaces has been studied for Hertzian contacts by Greenwood and Williamson [45] and for JKR contacts [11] by Fuller and Tabor [29]. Maugis [67] extended the DMT theory to elastic contacts of rough surfaces. DMT contacts include the extraload due to adhesion around the contacts. This extraload acts in addition to the applied load and thus increases the friction force [67].

## 5. CONCLUSION

A review is presented of microscale elastic and elastoplastic adhesion contact mechanics in MEMS and NEMS. Special emphasis is placed on discussion of some governing dimensionless parameters such as Tabor number, adhesion parameter, and peel number. Peel number is modified for the case of contact between rough surfaces. Roughness ratio, which is widely used in fluid mechanics, is introduced to characterize the relative importance of surface roughness for microscale adhesion contact in MEMS. Three kinds of asperity height distributions are discussed: Gaussian, fractal and exponential distributions. Both Gaussian and exponential distributions are shown to be special cases of fractal distribution. Casimir force induced adhesion in NEMS, and adhesion of carbon nanotubes with the substrate are also discussed. Finally, microscale plastic adhesion contact theory is briefly reviewed, and it is shown that the dimensionless number, the plasticity index in

various forms, can be expressed by the roughness ratio. Therefore, roughness ratio is an important dimensionless number to characterize the influence of surface asperities on mechanical behavior of MEMS.

The outstanding issues in the field include the micromechanical process of making and breaking of adhesion contact, the MEMS structural members' adhesion by inertia forces (as shown in Fig. 4), the coupling of physical (e.g. humidity, thermal, electromagnetic, mechanical, etc.) interactions, the trans-scale (nano-micro-macro) mechanisms of adhesion contact, adhesion hysteresis, as well as new effective ways of adhesion control in MEMS/NEMS. Work addressing these issues will help to understand the fundamental physics of microscale adhesion and the emerging concepts of nanoscale adhesion.

**REFERENCES**

1. S. M. Spearing, *Acta Mater.* **48**, 179 (2000).
2. R. Maboudian, *Surface Sci. Reports* **30**, 207 (1998).
3. R. Maboudian, W. R. Ashurst and C. Carraro, *Sensors Actuators* **A82**, 219 (2000).
4. R. Maboudian and R. T. Howe, *J. Vac. Sci. Technol.* **B15**, 1 (1997).
5. Y.-P. Zhao, *Arch. Appl. Mech.* **72**, 77 (2002).
6. L. X. Zhang, J. W. Zhang, Y.-P. Zhao and T. X. Yu, *Int. J. Nonlinear Sci. Num. Simul.* **3**, 353 (2002).
7. S. L. Miller, M. S. Rodgers, G. La Vigne, J. J. Sniegowski, P. Clews, D. M. Tanner and K. A. Peterson, *Microelectronics Reliability* **39**, 1229 (1999).
8. M. P. de Boer and T. A. Michalske, *J. Appl. Phys.* **86**, 817 (1999).
9. K. L. Johnson, *Proc. Institution Mech. Engineers* **C214**, 11 (2000).
10. R. S. Bradley, *Philosophical Magazine* **13**, 853 (1932).
11. K. L. Johnson, K. Kendall and A. D. Roberts, *Proc. Royal Soc. London* **A324**, 301 (1971).
12. D. Tabor, *J. Colloid Interface Sci.* **58**, 2 (1977).
13. K. L. Johnson, *Proc. Royal Soc. London* **A453**, 326 (1997).
14. V. M. Muller, Yu. S. Yushchenko and B. V. Derjaguin, *J. Colloid Interface Sci.* **77**, 91 (1980).
15. J. A. Greenwood, *Proc. Royal Soc. London* **A453**, 1277 (1997).
16. K. L. Johnson and J. A. Greenwood, *J. Colloid Interface Sci.* **192**, 326 (1997).
17. K. L. Johnson, *Tribology Intl.* **31**, 413 (1998).
18. B. Cappela and G. Dietler, *Surface Sci. Reports* **34**, 1 (1999).
19. B. V. Derjaguin, V. M. Muller and Yu. P. Toporov, *J. Colloid Interface Sci.* **53**, 314 (1975).

20. D. Maugis, *J. Colloid Interface Sci.* **150**, 243 (1992).
21. E. Meyer, R. M. Overney, K. Dransfeld and T. Gyalog, *Nanoscience: Friction and Rheology on the Nanometer Scale.* World Scientific, Singapore (1998).
22. D. Maugis and M. Barquins, *J. Phys. D: Appl. Phys.* **11**, 1989 (1978).
23. J. Israelachvili, in: *Fundamentals of Friction*, I. L. Singer and H. M. Pollock (Eds), NATO ASI Series E, Vol. 220. Kluwer, Dordrecht (1992).
24. B. J. Briscoe and S. L. Kremnitzer, *J. Phys. D: Appl. Phys.* **12**, 505 (1979).
25. R. W. Carpick, N. Agrait, D. F. Ogletree and M. Salmeron, *Langmuir* **12**, 3334 (1996).
26. M. A. Lantz, S. J. O'Shea, M. E. Welland and K. L. Johnson, *Phys. Rev.* **B55**, 10776 (1997).
27. P. Attard and J. L. Paker, *Phys. Rev.* **A46**, 7959 (1992).
28. H. Schlichting, *Boundary Layer Theory*, 7th edn. McGraw-Hill Book Company, New York (1979).
29. K. N. G. Fuller and D. Tabor, *Proc. Royal Soc. London* **A345**, 327 (1975).
30. C. Gui, M. Elwenspoek, N. Tas and J. G. E. Gardeniers, *J. Appl. Phys.* **85**, 7448 (1999).
31. C. H. Mastrangelo and C. H. Hsu, *J. Microelectromechanical Systems* **2**, 44 (1993).
32. L. S. Wang and Y.-P. Zhao, *Tribology* **22**, 339 (2002) (in Chinese).
33. T. S. Chow, *Phys. Rev. Lett.* **86**, 4592 (2001).
34. K. R. Morris, S. L. Nail, G. E. Peck, S. R. Byrn, U. J. Griesser, J. G. Stowell, S. J. Hwang and K. Park, *Pharmaceutical Science and Technology Today* **1**, 235 (1998).
35. M. Bordag, U. Mohideen and V. M. Mostepanenko, *Phys. Reports* **353**, 1 (2001).
36. H. B. Chan, V. A. Aksyuk, R. N. Kleiman, D. J. Bishop and F. Capasso, *Science* **291**, 1941 (2001).
37. E. M. Lifshitz, *Sov. Phys. JETP* **2**, 73 (1956).
38. M. Bostrom and B. E. Sernelius, *Phys. Rev.* **B61**, 2204 (2000).
39. Y.-P. Zhao and W. J. Li, *Chin. Phys. Lett.* **19**, 1161 (2002).
40. E. Buks and M. L. Roukes, *Phys. Rev.* **B63**, 033402 (2001).
41. J. N. Israelachvili, *Intermolecular and Surface Forces*, 2nd edn. Academic Press, London (1991).
42. F. M. Serry, D. Walliser and G. J. Maclay, *J. Appl. Phys.* **84**, 2501 (1998).
43. M. F. Yu, T. Kowalewski and R. Ruoff, *Phys. Rev. Lett.* **86**, 87 (2001).
44. J. P. Salvetat, G. A. D. Briggs, J. M. Bonard, R. R. Bacsa, A. J. Kulik, T. Stöckli, N. A. Burnham and L. Forró, *Phys. Rev. Lett.* **82**, 944 (1999).
45. J. A. Greenwood and J. B. P. Williamson, *Proc. Royal Soc. London* **A295**, 300 (1966).
46. I. M. Hutchins, *Tribology: Friction and Wear of Engineering Materials.* Edward Arnold, London (1992).
47. J. Larsson, B. Biwa and B. Storakers, *Mech. Mater.* **31**, 29 (1999).
48. J. H. Horng, *ASME Trans. J. Tribology* **120**, 82 (1998).
49. D. Dowson, *History of Tribology*, 2nd edn. Professional Engineering Publishing, London (1998).
50. R. A. Onions and J. F. Archard, *J. Phys. D: Appl. Phys.* **6**, 289 (1973).
51. B. Bhushan, *Principles and Applications of Tribology.* John Wiley & Sons, New York (1999).
52. D. J. Whitehouse and J. F. Archard, *Proc. Royal Soc. London* **A316**, 97 (1970).
53. Q. Zhao and F. E. Talke, *ASME Trans. J. Tribology* **122**, 269 (2000).
54. A. Kapoor, J. A. Williams and K. L. Johnson, *Wear* **175**, 81 (1994).
55. A. Kapoor, K. L. Johnson and J. A. Williams, *Wear* **200**, 38 (1996).
56. Z. Handzel-Powierza, T. Klimczak and A. Polijaniuk, *Wear* **154**, 115 (1992).
57. D. Maugis and H. M. Pollock, *Acta Metall.* **32**, 1323 (1984).
58. S. K. R. Chowdhury and H. M. Pollock, *Wear* **66**, 307 (1981).
59. Y.-P. Zhao and T. X. Yu, *Int. J. Nonlinear Sci. Num. Simul.* **1**, 361 (2000).
60. L. P. Buchwalter, *J. Adhesion* **72**, 269 (2000).
61. G. Binnig and H. Rohrer, *Rev. Modern Phys.* **71**, S324 (1999).
62. F. Q. Yang, *Appl. Phys. Lett.* **80**, 959 (2002).
63. H. Gao, Y. Huang and W. D. Nix, *Naturwissenschaften* **86**, 507 (1999).

64. Y.-P. Zhao, in: *Advances in Plasticity and Geodynamics — 80th Anniversary Volume in Honor of Academician Ren Wang*, B. Xu and Z. P. Huang (Eds), p. 87. World Publishing Corporation, Beijing (2000) (in Chinese).
65. J. R. Barber and M. Ciavarella, *Int. J. Solids Structures* **37**, 29 (2000).
66. A. Majumdar and B. Bhushan, *ASME Trans. J. Tribology* **113**, 1 (1991).
67. D. Maugis, *J. Adhesion Sci. Technol.* **10**, 161 (1996).

## APPENDIX

List of symbols

| | |
|---|---|
| $a$ | contact radius, separation of two plates |
| $a, b$ | semi-minor and semi-major radii of elliptical contact |
| $A$ | Hamaker constant |
| $A_r$ | real contact area |
| $b, c$ | parameters in equation (15) and Table 3 |
| $c$ | speed of light |
| $C$ | constant in equation (23) |
| $d$ | separation of smooth plane with respect to reference plane of mean asperity height |
| $e$ | eccentricity of ellipse |
| $E$ | Young's modulus |
| $E^*$ | equivalent Young's modulus |
| $E(e)$ | complete elliptical integral of the second kind |
| $E_{\text{Casimir}}$ | Casimir energy |
| $E_{\text{vdW}}$ | van der Waals energy |
| $f(\theta)$ | dimensionless roughness function defined in equation (25) |
| $F(a)$ | Casimir force acting between two parallel plates in vacuum |
| $h$ | suspension height of cantilever beam from substrate, indentation depth |
| $h_0$ | equilibrium distance in Fig. 5, reference indentation depth in equation (57) |
| $h^*$ | neck height in the JKR model in equation (4) |
| $H$ | hardness of material |
| $K(e)$ | complete elliptical integral of the first kind |
| $L$ | characteristic length, length of cantilever beam or doubly clamped beam |
| $L_{\text{max}}$ | maximum length of cantilever beam that will not adhere to substrate |
| $n$ | number of asperities per unit area in contact with smooth surface |

| $N$ | number of asperities per unit area |
|---|---|
| $N_P$ | peel number |
| $\bar{N}_P$ | peel number for rough contact |
| $p_s$ | shakedown limit load |
| $P$ | applied load |
| $P_c$ | pull-off force |
| $\bar{P}$ | ratio between total load and adhesion part of load |
| $P^*$ | dimensionless total compressive load per unit area |
| $q(x)$ | load in Fig. 12 |
| $R$ | radius of curvature, equivalent radius |
| $R_m$ | mean effective radius of curvature of asperities |
| $R_P$ | radius of circular plate |
| $(R_P)_{max}$ | maximum radius of circular plate that will not adhere to substrate |
| $R_x, R_y$ | effective radii of curvature in the principal $x$ and $y$ planes |
| $s$ | crack length, $s = d/\sigma$, shape coefficient in equation (43) |
| $s_e$ | equilibrium separation |
| $S$ | area of plates |
| $S_f$ | surface force |
| $S_H$ | contact stiffness using Hertz contact theory |
| $S_{JKR}$ | contact stiffness using JKR contact theory |
| $t$ | thickness of cantilever beam |
| $u(x)$ | deflection of cantilever beam in Fig. 6 |
| $U$ | interaction energy of van der Waals force per unit area |
| $U_E, U_S$ | elastic energy and detachment energy of cantilever beam |
| $U'_{Sp}$ | mechanical work for separating two bonded surfaces from equilibrium to infinity |
| $w$ | width of square plate |
| $w_0$ | initial separation between strip and substrate in Fig. 12 |
| $w(x)$ | deflection of strip in Fig. 12 |
| $w_{max}$ | maximum of square plate that will not adhere to substrate |
| $W_a$ | Dupré adhesion or work of adhesion |
| $W'_C$ | effective adhesion considering surface roughness |
| $W_{sn}$ | work of adhesion between MWCNT and $SiO_2$ substrate |
| $x$ | $z/\sigma$ |
| $\alpha$ | roughness exponent |
| $\beta$ | dimensionless parameter in equation (31) |

| | |
|---|---|
| $\beta^*$ | correlation distance between asperities |
| $\gamma$ | surface energy |
| $\gamma_g$ | surface energy of graphite |
| $\gamma_{SiO_2}$ | surface energy of $SiO_2$ substrate |
| $\Gamma$ | gamma function |
| $\delta_0, \delta_1$ | deformation due to adhesion, elastic compression |
| $\delta_c$ | maximum extension of asperity |
| $\varepsilon$ | interatomic spacing |
| $\theta$ | adhesion parameter |
| $\lambda$ | elasticity parameter ($\lambda = 1.157\mu$), retardation length |
| $\lambda'$ | $0.5\mu^{3/2}$ |
| $\mu$ | Tabor number |
| $\mu_D$ | $2.921\mu$ |
| $\mu_T$ | $3.898\mu$ |
| $\nu$ | Poisson's ratio |
| $\xi$ | correlation length of the self-affine fractal surface |
| $\Xi$ | roughness ratio defined in equation (6) |
| $\Xi_m$ | average roughness ratio |
| $\sigma$ | standard deviation of the distribution of asperity heights |
| $\sigma_0$ | parameter defined in Table 1 |
| $\sigma_R$ | residual stress |
| $\sigma_Y$ | yield stress |
| $\varphi(z)$ | Gaussian distribution |
| $\phi(z)$ | exponential distribution |
| $\psi(z)$ | asperity height distribution of a fractal surface |
| $\psi_0$ | parameter defined in equation (28) |
| $\Psi$ | plasticity index |
| $\Psi^*$ | plasticity index suggested by Onions and Archard in equation (40) |
| $\Psi_c$ | plasticity index for 'cylinder-on-plane' contact |
| $\Psi_s$ | repeated sliding plasticity index |
| $\omega_p$ | plasma frequency |
| $\hbar$ | Planck's constant divided by $2\pi$ |